The ephemeral development of C' shear bands: a numerical modelling approach

Finch, M. A.[a,b]*, Bons, P. D.[a], Steinbach, F.[a], Griera, A.[c], Llorens, M.-G.[d], Gomez-Rivas, E.[e], Ran, H. [a,f], and de Riese, T.[a]

[a]Department of Geosciences, Eberhard Karls University Tübingen, 72074 Tübingen, Germany.
[b]School of Earth, Atmosphere and Environment, Monash University, Clayton, Victoria, 3800, Australia.
[c]Departament de Geologia, Universitat Autònoma de Barcelona, 08193 Bellaterra, Spain
[d]Institute of Earth Sciences Jaume Almera (ICTJA-CSIC), Lluís Solé Sabarís s/n, E-08028 Barcelona, Spain
[e]Departament de Mineralogia, Petrologia i Geologia Aplicada, Facultat de Ciències de la Terra, Universitat de Barcelona, Martí i Franquès s/n, 08028 Barcelona, Spain
[f]School of Earth Sciences and Resources, China University of Geosciences, Beijing, 100083, China.

*Corresponding author. Current address: School of Earth, Atmosphere and Environment, Monash University, Clayton, Victoria, 3800, Australia.

Abstract

C' shear bands are ubiquitous structures in shear zones but their development is poorly understood. Previous research has determined they mostly occur in rocks with a high mechanical strength contrast. Using numerical models of viscoplastic deformation, we studied the effect of the proportion of weak phase and the phase strength contrast on C' shear band development during simple shearing to a finite strain of 18. We found that C' shear bands form in models with ≥5% weak phase when there is a moderate or high phase strength contrast, and they occur in all models with weak phase proportions ≥15%. Contrary to previous research, we find that C' shear bands form when layers of weak phase parallel to the shear zone boundary rotate forwards. This occurs due to mechanical instabilities that are a result of heterogeneous distributions of stress and strain rate. C' shear bands form on planes of low strain rate and stress, and not in sites of maximum strain rate as has previously been suggested. C' shear bands are ephemeral and they either rotate backwards to the C plane once they are inactive or rotate into the field of shortening and thicken to form X- and triangle- shaped structures.

1. Introduction

C' shear bands are a common feature of shear zones in nature (Fig. 1), experiments, and models (e.g., White, 1979; Platt and Vissers, 1980; Platt, 1984; Dennis and Secor, 1987) and are used as kinematic indicators in shear zones (e.g., Dennis and Secor, 1987), despite persistent debate as to their origin and development (e.g., Xypolias, 2010). Also known as extensional crenulation cleavage (Platt and Vissers, 1980; Platt, 1984; Dennis and Secor, 1987), C' shear bands dip at an angle of 15–35° to the shear zone boundary (SZB) in the direction of shear (Fig. 1; White, 1979; Platt and Vissers, 1980). They are typically associated with an S-C fabric in which the main S-foliation dips at low angle to the SZB and in the opposite direction relative to the shear-sense, while C shear planes are parallel to the SZB (Berthé et al., 1979). C' shear bands show a synthetic shear sense and cut across S and C planes at an oblique angle, which has led to the suggestion that they form late in the deformation history (Platt and Vissers, 1980). C' shear bands may appear in concert with rare, conjugate C'' shear bands, which dip in the opposite direction and have an antithetic shear sense (Simpson and De Paor, 1993; Law et al., 2004; Little et al., 2011). C'' shear bands are thought to develop under general shear and rotate toward the flow plane while inverting their shear sense (Grasemann et al., 2003; Gomez-Rivas et al., 2007).

The relationship between the orientation of C' shear bands and the geometry of flow is widely debated. Studies of natural shear zones have shown that C' shear bands commonly nucleate parallel to the acute bisector of the flow eigenvectors, which is the plane of maximum antithetic shear strain rate (Platt and Vissers, 1980; Simpson and De Paor, 1993; Klepeis et al., 1999; Law et al., 2004; Kurz and Northrup, 2008; Gillam et al., 2013). Planes at this angle rotate backwards toward parallelism with the shear zone, in which case C' shear bands would be expected at all angles between the acute bisector and the extensional eigenvector (Simpson and De Paor, 1993; Gillam et al., 2013). Alternatively, C' shear bands have been interpreted as representing flow parallel to the inclined (shortening) eigenvector due to bulk hardening (Bobyarchick, 1986) or general shear (Simpson and De Paor, 1993), in which case they would be stable at a vorticity number of $W_k \sim 0.6–0.8$
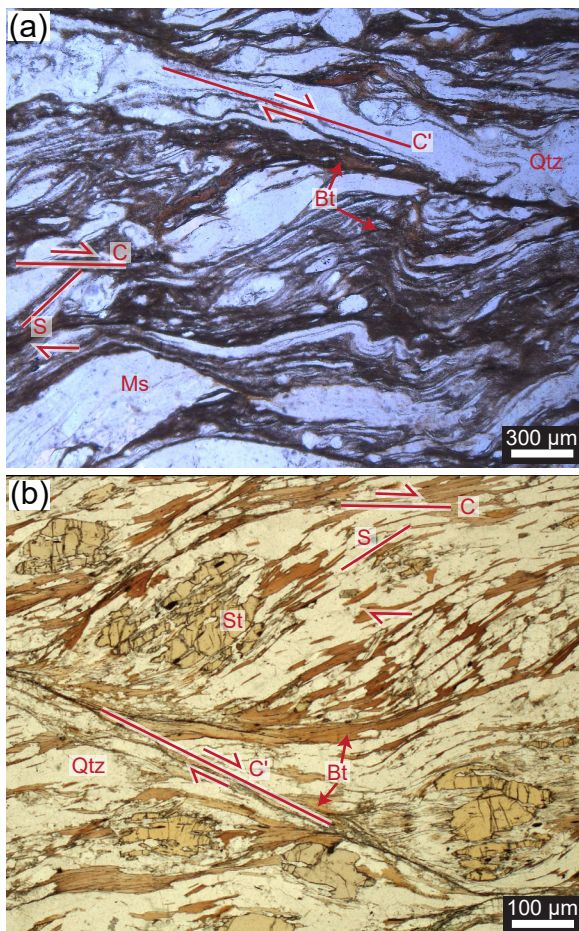
Fig. 1. Photomicrographs of microstructures in sheared polyphase rocks from the Zanskar Shear Zone in NW Himalaya. C' shear bands are defined by biotite and quartz.

(Grasemann et al., 2003). Other theories suggest that C' shear bands form on planes parallel to an idealised Coulomb failure surface in low-grade rocks (Blenkinsop and Treloar, 1995), on pre-existing joints (Pennacchioni and Mancktelow, 2007), or parallel to the direction of maximum finite shear strain (Ramsay and Lisle, 2000), a suggestion that is supported by the observation that they occasionally consist of fine-grained, recrystallised material (e.g., Ji et al., 2004; Finch et al., 2017).

While common to shear zones at all scales, C' shear bands do not form in all rock types. They are most common in well-foliated rocks such as schist and phyllite (Passchier, 1991; Delle Piane et al., 2009) and the presence of a weak phase seems to be required for their development (Wilson, 1984; Goodwin and Tikoff, 2002). A weak phase may be the result of the development of a crystallographic preferred orientation in one or more phases (Dillamore et al., 1979; Llorens et al., 2016a; 2017), the presence of a mineral with lower strength than other phases (Jordan, 1987; Holyoke and Tullis, 2006), the presence of partial melt (Rosenberg and Handy, 2005; Holtzman and Kohlstedt, 2007) or in monomineralic rocks the presence of one slip system significantly weaker than the others (Goodwin and Tikoff, 2002; de Riese, 2019). The proportion of weak phase does not need to be high, with some suggesting that trace amounts are sufficient (Goodwin and Tikoff, 2002). It is likely constrained by the amount required to form an interconnected layer or network, which would enable the development of a strong anisotropy, a factor that seems to be important for the development of C' shear bands (Platt and Vissers, 1980; Platt, 1984; Jordan, 1987; Williams and Price, 1990). The persistent controversy over the conditions that lead to development of C' shear bands is partly because many studies are based on naturally-deformed rocks, in which parameters such as the initial orientation of the shear bands, the strain and strain rate distribution, and any widening or thinning of the shear zone are difficult to determine (Passchier, 1991; Gillam et al., 2013). Experimental work is better able to control these variables. Experimental studies that have varied the strength ratio between strong and weak phases suggest that C' shear bands form when the ratio is at least 3 to 5 (Jordan, 1987; Stünitz and Tullis, 2001; Holtzman et al., 2003; Holyoke and Tullis, 2006). The minimum amount of weak phase required has been suggested to be ~20% (Jordan, 1987), but this has not been systematically evaluated. Experimental studies may be able to elucidate the variables that lead to the development of C' shear bands but they can only provide limited information on the processes that occur during shearing because rocks cannot be observed during deformation. Moreover, the length and time scales are limited in experiments. Numerical models overcome these limitations and provide continuous observation of the evolution of the system up to high strain. Moreover, they can also be used to provide information on stress and strain rate distribution at every step of the simulation, offering a powerful insight into the processes that occur in deforming rocks.

Previous numerical studies on shearing in polyphase rocks have focussed on the effect of varying proportions and sizes of hard and soft phases in two-phase microstructures (e.g., Bons and Cox, 1994; Jessell et al., 2009; Dabrowski et al., 2012; Cyprych et al., 2016; Steinbach et al., 2016; Gardner et al., 2017; Ran et al., 2018; Llorens et al., 2019) or on mechanical anisotropy in single-phase materials (Llorens et al., 2016a; 2017; de Riese, 2019; Ran et al., 2019). These studies have demonstrated that S-C and S-C' fabrics form when strain localises, which depends on the presence of a weak phase and/or a strong mechanical anisotropy. Our work in this paper builds on these studies, simulating the microstructural development of a three-phase aggregate (as shear bands are commonly observed in rocks composed dominantly of feldspar, quartz and mica) and manipulating the proportion and strength of weak phase to investigate how C' shear bands develop.

2. Method
2.1. The ELLE+VPFFT code

We investigated the factors that lead to development of C' shear bands using the numerical modelling platform ELLE, which is designed to simulate microstructural development during deformation (http://www.elle.ws; Jessell et al., 2001; Bons et al., 2008). Grains or phase regions in the ELLE microstructure are polygons (known as flynns) that are defined by boundary nodes (bnodes) connected with straight lines forming double or triple junctions (Fig. 2). The model also employs a grid of unconnected nodes (unodes) that store additional information about the microstructure, such as local lattice orientation or state variables, including

the local strain rate and stress state (Fig. 2). In the simulations presented here, the ELLE platform is coupled to the full-field viscoplastic deformation code (VPFFT) of Lebensohn (2001). In the VPFFT-method, deformation is assumed to be accommodated by dislocation glide on crystallographic slip systems. Each element in the model (represented by a unode) is regarded as a crystallite of a mineral phase with its own crystallographic properties and symmetry, and with a certain lattice orientation that can evolve with deformation. The glide along a slip system is described as simple shear ($\dot{\gamma}_s$) parallel to that slip system (s):

$$\dot{\gamma}_s = A\left(\frac{\sigma_{//s}}{\tau_s}\right)^n \qquad (1)$$

Here A is the pre-exponential rate factor, set to unity for all phases and all slip systems in this paper. $\sigma_{//s}$ is the deviatoric shear stress parallel to the slip-system s, and n the stress exponent, set to three here. The critical resolved shear stress, τ_s, is a viscous term that determines the effective strength or resistance to shear of the slip system s. The mechanical properties of a phase are thus determined by its crystallographic properties and the τ_s-values for each of the available slip systems. The VPFFT-code calculates the stress and velocity fields by summing the shear components along all slip systems and all elements that result in the least work rate for the given boundary conditions and local stress and strain-rate compatibility requirements. The method employs a Fast Fourier Transform (FFT) for the spectral solver of the visco-plastic deformation, hence the name "VPFFT". Details of the VPFFT method in general can be found in Lebensohn (2001), Lebensohn et al. (2008; 2009), and Montagnat et al. (2014) and on the coupling with the ELLE-code in Griera et al. (2013), Llorens et al. (2016a;b; 2017), Steinbach et al. (2016) and Gomez-Rivas et al. (2017).

The spectral VPFFT solver requires a regular grid of NxM elements, whereby N and M must be a power of two. For all simulations presented here, $N=M=256$ was used. Another requirement is that the model boundaries are periodic, that is, a material point that leaves the model on one side, enters it on the opposite side (Fig. 2a-c). The displacement of material points and bnodes that define phase boundaries is calculated by interpolation of the velocity field and by linear integration for the given (small) time step. During deformation, the position of material points will deviate from the regular grid (Fig. 2b). After one deformation step, all material points are repositioned into a new square unit cell (Fig. 2c), taking advantage of the periodic boundaries. Properties (phase and lattice orientations) of the unodes in the rectangular grid are interpolated from those of material points (Griera et al., 2011; 2013).

2.2. Visualisation

For every time step, the ELLE+VPFFT code records a wealth of data. For visualisation here we only use the phase distribution as recorded by the flynns and the stress and strain-rate distri-
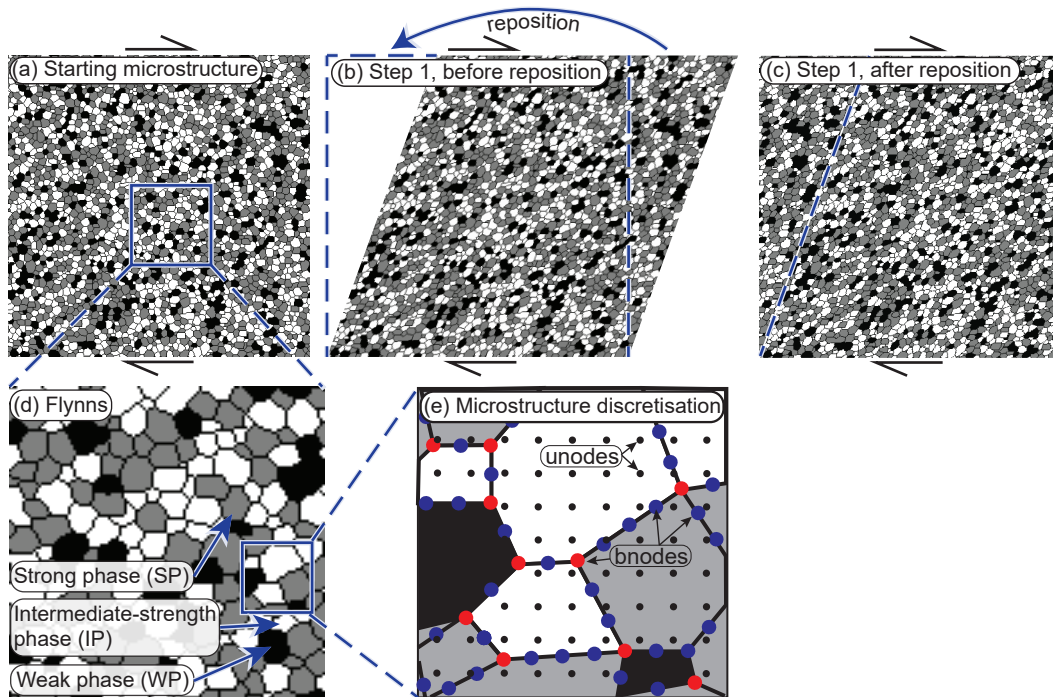

Fig 2. Basic process of microstructure simulation. (a) The starting microstructure consists of three grain types that undergo one increment of γ = 0.02 dextral shear. (b) The microstructure is deformed with wrapping boundaries. (c) The microstructure is repositioned back to a square before the next increment of strain. (d) Zoom in of (a) showing the three flynn (grain) types: strong phase (SP), intermediate-strength phase (IP), and weak phase (WP). (e) Zoom-in of (d) showing that flynn grain boundaries are defined by double (blue) and triple (red) bnodes joined by straight lines. An additional grid of unconnected nodes (unodes, black) is overlain on flynns and stores state variables and flynn properties.

bution. The VPFFT code provides the deviatoric stress (S_{ij}) and strain-rate ($\dot{\varepsilon}_{ij}$) tensors for each unode in the model and for each time step. As it is impractical to provide the six components of both symmetric tensors, we provide the von Mises stress and strain rate, normalised to the mean value for the whole model. The von Mises stress (S_{VM}) or strain rate ($\dot{\varepsilon}_{VM}$) is given by:

$$S_{VM} = \sqrt{\tfrac{2}{3} S_{ij} S_{ij}} \quad \text{and} \quad \dot{\varepsilon}_{VM} = \sqrt{\tfrac{2}{3} \dot{\varepsilon}_{ij} \dot{\varepsilon}_{ij}} \tag{2}$$

2.3. Implementation to simulate C' shear band development

To investigate the factors that lead to development of C' shear bands we used a three-phase microstructure and modified the proportion and strength of a weak phase (WP) with respect to an intermediate-strength phase (IP) and a strong phase (SP) (see Table 1). Starting models were square and defined by 2,748 equant grains with a random distribution of the three phases (Fig. 3a). Velocity boundary conditions with constant strain rate were applied with top-to-the-right (dextral) simple shear in increments of $\Delta\gamma = 0.02$, up to a finite shear strain of $\gamma=18$ in 900 steps. After each deformation step, the model was repositioned to the initial square unit cell and grain properties mapped back on to the grid before the next deformation step. A power-law viscous rheology (Eq. 1) was employed with $n = 3$.

Each phase was associated with a mineral model that specified the slip systems and their effective strength or resistance to shear, τ_s. The mineral models employed in this study attempted to broadly approximate the most important features of mica (WP), quartz (IP), and feldspar (SP) in order to more closely correspond to previous experimental work on three-phase aggregates (Holyoke and Tullis, 2006). To model the WP we used a mineral model with hexagonal symmetry and three slip systems (basal, prismatic, and pyramidal), as was done by Griera et al. (2011; 2013) and Ran et al. (2018; 2019). Although mica is monoclinic, it is pseudohexagonal and its most important mechanical feature is an easy glide plane since shear in mica is easier parallel to the basal plane than in any other direction. Accordingly we set $\tau_{WP,basal}$ at one tenth of both $\tau_{WP,non-basal}$, producing a mechanically anisotropic WP. Feldspar is also pseudohexagonal, so we employed a hexagonal mineral model for the SP, but set the effective strength of all its slip systems to the same τ_{SP}. For the IP we used the crystal model of quartz with four slip systems (basal, prismatic, pyramidal <a> and pyramidal <c+a>) and gave the effective strength of all four slip systems the same value τ_{IP}. This made the IP effectively mechanically isotropic (Griera et al., 2011; 2013).

Two variables were investigated (see Table 1): (1) the starting proportion of weak phase relative to the two other phases (producing four basic conditions described below), and (2) the difference in effective strength between the WP, IP and SP (termed strength contrast: high, medium, or low; Table 1), giving 12 simulations in total. The starting proportion of WP was set at 5% (condition name: 5WP), 15% (15WP), 30% (30WP) or 45% (45WP). This proportion changed during a simulation as small grains of the WP smeared out so much that their width became less than the unode-grid could resolve, and they were therefore removed from the model (see table S1 in the supplementary material). In all simulations we used $\tau_{WP,non-basal} = 10$ x $\tau_{WP,basal}$ and $\tau_{SP} = 2$ x τ_{IP}. To investigate the effect of the overall strength contrast between the WP and stronger phases, we present three cases: (i) low phase strength contrast ($\tau_{IP} = 15$ x $\tau_{WP,basal}$), (ii) medium phase strength contrast ($\tau_{IP} = 25$ x $\tau_{WP,basal}$), and (iii) high phase strength contrast (τ_{IP}

Table 1. The phase strength contrasts and proportion of weak phase in each of the 12 models in this study. WP = weak phase, IP = intermediate strength phase, SP = strong phase.

| | | | Proportion of WP | | |
		5	15	30	45
	IP 15x SP 30x	5WP_Low	15WP_Low	30WP_Low*	45WP_Low
Strength of phases relative to WP basal plane	IP 25x SP 50x	5WP_Med	15WP_Med*	30WP_Med	45WP_Med
	IP 40x SP 80x	5WP_High*	15WP_High	30WP_High	45WP_High*

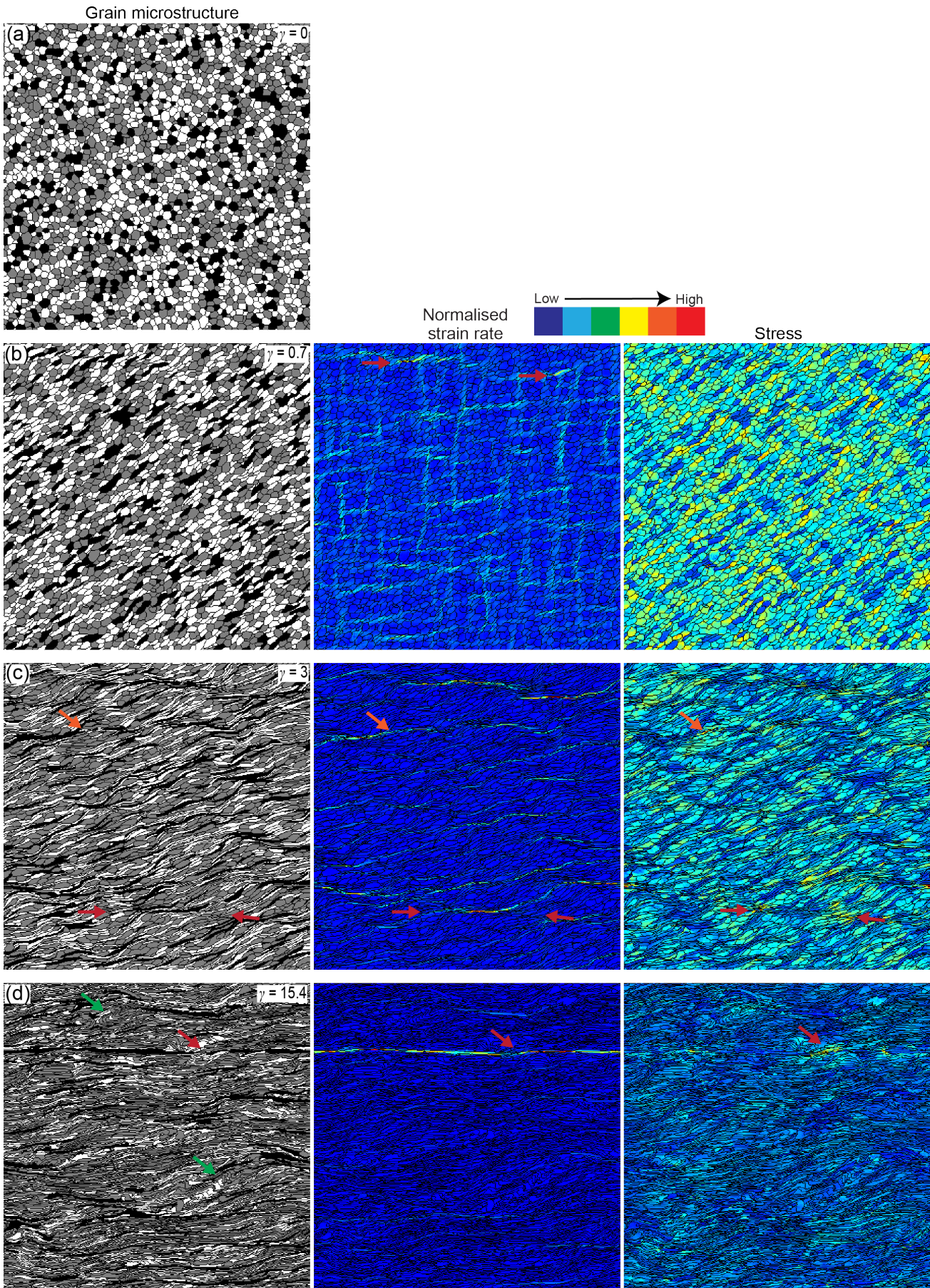*Denotes model movie supplied in the supplementary material

Fig. 3. Stages of microstructural development in the 15WP_Med model. (a) Starting microstructure, (b) stage 1: grain elongation and rotation. Note the distribution of maximum strain rate (red arrows) localised to tips of WP grains that are parallel to the C plane, (c) stage 2: S-C fabric development. Stress is highest in the IP+SP adjacent to high strain rate layers of interconnected WP (red and orange arrows). (d) stage 3: shear band development and strain partitioning. Maximum stress in the model is in the gap in the shear band (red arrow). Green arrows highlight areas that have been asymmetrically folded (c.f. Fig. 1a). The first column shows the grain microstructure, the second column shows the normalised von Mises strain rate and the third column shows the von Mises stress. Images in the same row correspond to the same model and step.

Table 2. The effective strength of the phases in the three phase strength contrast conditions. All slip systems within a phase were set to the same value, except for the weak phase which has a basal plane weaker than its other planes.

	Low PSC	Medium PSC	High PSC
WP_{basal}	1	1	1
$WP_{non-basal}$	10	10	10
IP	15	25	40
SP	30	50	80

$= 40 \times \tau_{WP,basal}$; Table 2) .

3. Results

Movies of the evolution of the microstructure, the von Mises strain rate and von Mises stress distributions as a function of shear strain are presented in the supplementary material and listed in Table 1. The microstructure depicts grain shapes and distributions with the weak phase shown in black, the intermediate-strength phase in white, the strong phase in grey, and grain boundaries in dark grey. We first describe the general microstructural evolution of the models followed by a description of how these structures evolve differently in models with different WP proportions and strengths. We then describe the appearance of C' shear bands in the models and the conditions in which they form.

3.1. Microstructural evolution and systematic variations between models

The microstructural evolution of the simulations can be separated into three main stages (Fig. 3a-d): (1) grain elongation and rotation (Fig. 3b), (2) S-C fabric development (Fig. 3c), and (3) shear band development and strain partitioning (Fig. 3d). All stages appear in all simulations to different extents, but the processes within each stage and the timing of each process varies between simulations. While there is systematic variation in the timing of the stages between simulations, there is also local variation in situations where, for example, several grains of WP happen to be in alignment in the starting microstructure in a particular simulation, which causes earlier development of shear bands. Additionally, the three stages of microstructural evolution progress slowly as strain increases, so while it could be interesting to compare the timing of each stage between models, defining the boundaries of each stage would be subjective and imprecise. However, where useful we compare the microstructural development of models at the same finite strain (γ) to illustrate how structures evolve differently under different WP proportions and relative strengths. We first describe each microstructural stage before discussing the differences between the models.

3.1.1. Grain elongation and rotation

The first stage in the microstructural development of the models is an increase in the axial ratio of the grains with their long axes defining the developing S foliation. WP grains flatten and then form lozenge and fish shapes with tips parallel to the SZB (Fig. 3b). Grains of IP and SP also show elongation and asymmetry but at higher strains than the WP (Fig. 3c). Stress is highest between grains and layers of WP, causing them to link up and begin to form patches and discontinuous layers (Fig. 3b). S-plane parallel elongate grains and layers gradually rotate clockwise, toward the SZB, and the local strain rate is highest where the WP forms C
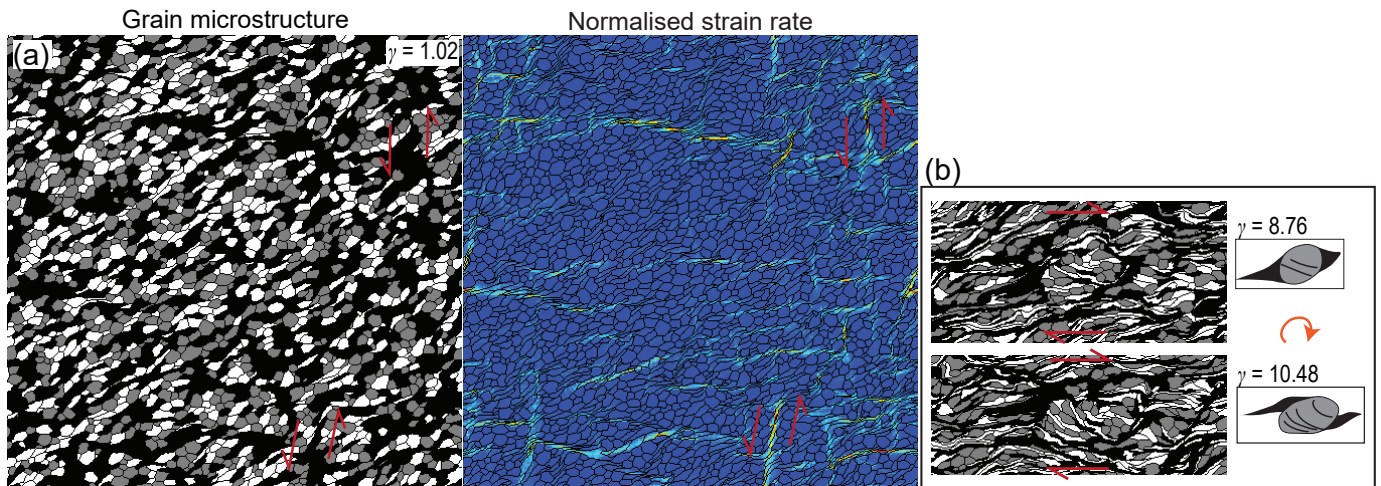

Fig. 4. Notable features of microstructural development. (a) Antithetic C'' shear bands in the early stages of shearing in the 45WP_High model. (b) Poorly formed σ- and δ- type objects in the 45WP_High model. Note that in the bottom panel the lithon shows extension and elongation compared to the top panel because the long axis has rotated into the extension direction.

planes (Fig. 3b, red arrows). In cases where multiple WP grains are in contact at the beginning of the simulation and aligned approximately vertically, they form a left-dipping band at a high angle to the SZB. These bands experience a high strain rate and show top-down, antithetic shearing forming C" shear bands (Fig. 4a). C" shear bands gradually rotate clockwise and antithetic shearing ceases once they are ~45° to the SZB, which generally occurs by $\gamma \sim 2.5$.

3.1.2. S-C fabric development

As layers of the WP rotate into parallelism with the C plane the microstructure transitions from the initial S (±C") fabric to an S-C fabric (Fig. 3c). The WP is the dominant phase that defines C planes, but grains of IP are also incorporated (Fig. 3c). Grains of WP and IP that are parallel to the C plane are elongate, flat and experience high strain rates (Fig. 3c). WP grains show a dominance of basal plane activity (relative to non-basal planes) with c-axes parallel to the y-axis (Fig. S1). Stress is high between layers of WP and highest between closely spaced layers and grains, which causes them to grow longer with increasing finite strain as more WP grains are incorporated in these layers (Fig. 3c red and orange arrows). The SP forms lozenge and σ-type objects with grain tips parallel or sub-parallel to the C plane (Fig. 3c). In regions where there is a high concentration of IP and SP between C plane parallel WP, the stronger phase areas act as lithons that experience low degrees of deformation (Fig. 4b).

3.1.3. Shear band development and strain partitioning

C plane-parallel WP layers localise strain rate and, if the layer becomes long and thick enough, can redistribute and localise all the strain in the model (Fig. 3d). We designate these layers 'shear bands' once they attain a length of half the model box. Although this distinction is somewhat arbitrary it is based on the observation that once WP layers reach these approximate lengths their strain rate increases as strain concentrates to these layers and decreases elsewhere. These shear bands increase in length with increasing strain, and occasionally form a layer of continuous WP that spans the entire model (Fig. 3d, see also supplementary material strain rate movie for 15WP_Med at 1:45). In some models these through-going shear bands partition all the strain and the rest of the model can become passive for the remainder of the simulation. However, such instances are rare, and the more common occurrence is that through-going shear bands partition most of the strain, but other discontinuous shear bands still show a non-zero strain rate. As these discontinuous shear bands accumulate grains of WP their strain rate increases, localising strain away from the through-going shear band. In the absence of through-going shear bands the strain rate distribution is more dynamic and the location of maximum strain rate jumps between layers of WP that are parallel to the SZB (e.g., see supplementary material strain rate movie for 30WP_Low).

At any point in the simulation shear bands typically contain segments parallel to the C plane as well as segments oriented up to 45° from the SZB (Fig. 5b,c). The orientation of shear bands as the simulation progresses is dynamic, that is, shear bands frequently rotate forwards and backwards. This is most pronounced in models with 30WP and 45WP, whereas models with 5WP and 15WP show a reduced rate of rotation at higher finite strains.

3.2. Differences in microstructural evolution between models

The microstructural evolution of the models changes as a function of the proportion of weak phase and the strength contrast between the phases. We consider the differences between models from low to high finite strain (summarised in Table 3).

The major difference between models up to $\gamma = 2$ is the presence or absence of antithetic (C") shear bands (Fig. 4a). All 30WP and 45WP models show antithetic shearing, but C" shear bands are more common and persist longer when there is a high strength contrast between phases, as was also observed by Ran et al. (2019) for two-phase aggregates. Antithetic shear bands only appear in the 15WP model in the high phase strength contrast condition and they do not appear in 5WP models.

Grain shape evolution also varies within and between models. The WP and IP become elongate and flat before the SP in all models (Fig. 3), but the extent to which the SP retains its equant shape varies
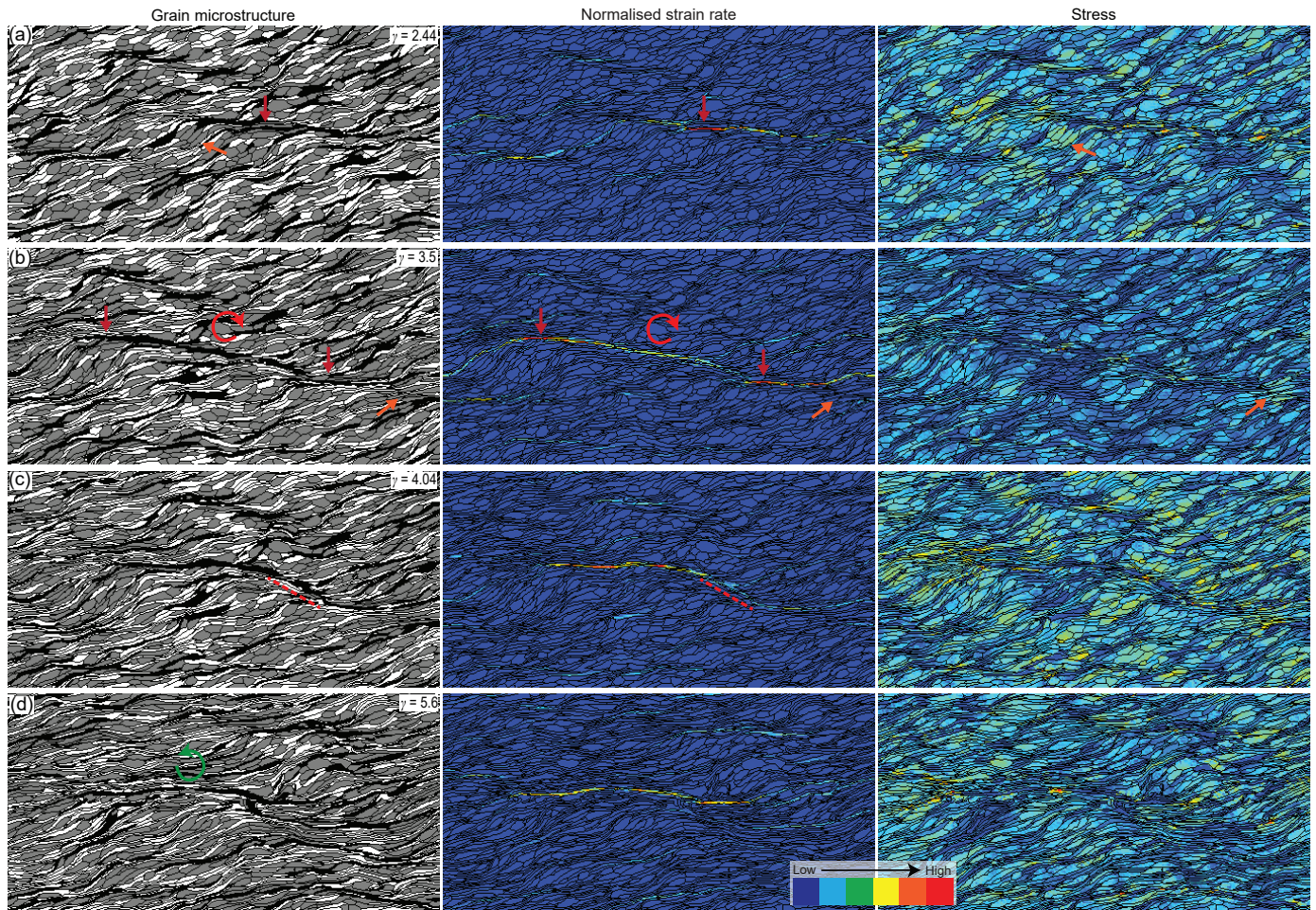
Fig. 5.The formation of C' shear bands by the rotation of a C plane forwards due to high strain rate in the shear band and high stress at the tip of the shear band. (a) Discontinuous shear band with section parallel to the SZB at high strain rate (red arrow) and high stress in the IP+SP region at the end of the shear band (orange arrow). (b) A low strain rate section in the shear band is bracketed on either side by high strain rate sections (red arrows) and begins to rotate forwards. (c) C' shear band forms in low strain rate section (red dashed line). (d) Strain rate reduces in the shear band and the C' shear band has rotated back into parallelism with the SZB and C planes. The first column shows the grain microstructure, the second column shows the normalised von Mises strain rate and the third column shows the von Mises stress. Model shown is 15WP_High and images in the same row correspond to the same model and step.

between models. When there is a low strength contrast the SP becomes flat and elongate relatively quickly (by γ ~ 6, see supplementary material grain microstructure movie for 30WP_low at 00:42) and there is little difference in grain shape between models with different proportions of weak phase. In contrast, at γ ~ 6 in the medium strength models, the 5WP and 15WP conditions show elongate and flat SP, whereas the 30WP and 45WP conditions show lozenge shaped and equant grains (see supplementary material grain microstructure movies at 00:42). When there is high strength contrast only the 5WP model contains flat and elongate grains of SP at γ ~ 6. The 45WP_High model retains equant SP grains and the 15WP_High and 30WP_High models show a mix of flat, lozenge and equant shapes.

While all models develop shear bands by γ = 18, the presence of through-going shear bands and the extent to which deformation partitions to shear bands differs between simulations. Simulations with a low strength contrast do not form through-going shear bands, whereas they develop in all medium and high strength contrast models (e.g., compare grain microstructure and strain rate movies in supplementary material for 5WP_High and 15WP_Med conditions). Additionally, in high strength contrast models strain rate more commonly partitions to a single shear band, rather than being distributed between several shear bands (e.g., see supplementary material strain rate movie for 5WP_High at 2:00). The proportion of WP also affects the strain rate distribution because a higher proportion of WP leads to the development of more shear bands to localise strain. When there are several shear bands the location of maximum strain rate switches between them over progressive model steps (e.g., see supplementary material strain rate movie for 30WP_Low at 2:00). In contrast, when there is a lower proportion of WP and only one or two shear bands can form, the locus of maximum strain rate will remain in the same location, within the one or two shear bands available

Table 3. Summary of major microstructural differences between simulation conditions

		Antithetic C" shear bands	SP shape at γ~6	C' shear bands	Through-going shear bands?	Strain partitions to multiple shear bands or just one?
Low PSC	5WP	No	Elongate and flat	No	No	Multiple
	15WP	No	Elongate and flat	Yes	No	Multiple
	30WP	No	Elongate and flat	Yes	No	Multiple
	45WP	No	Elongate and flat	Yes	No	Multiple
Medium PSC	5WP	No	Elongate and flat	Yes	Yes	Multiple
	15WP	No	Elongate and flat	Yes	Yes	Multiple
	30WP	Yes	Equant	Yes	Yes	Multiple
	45WP	Yes	Equant	Yes	Yes	Multiple
High PSC	5WP	No	Elongate and flat	Yes	Yes	One
	15WP	Yes	Equant	Yes	Yes	One
	30WP	Yes	Equant	Yes	Yes	One
	45WP	Yes	Equant	Yes	Yes	One

(e.g., see supplementary material strain rate movie for 5WP_High at 2:00). Thus, a higher proportion of weak phase results in more heterogenous distribution of strain rate, consistent with the two-phase numerical models of Gardner et al. (2019).

The 45WP_High model deserves separate consideration since it shows a number of microstructural features that are not observed in the other models. Rather than forming S-C-C' fabric, the WP in this model forms anastomosing shear bands around lithons of IP+SP (see supplementary material movie of grain microstructure for 45WP_High condition). These lithons are more resistant to deformation and rotate clockwise between shear bands of WP, consistent with the findings of Griera et al. (2011; 2013), Jammes et al. (2015), Meyer et al. (2017) and Ran et al (2018). This rotation causes the development of antithetic shear bands on high angle, left-dipping shear bands at high finite strain (γ ~ 9). This model also shows accumulations of WP in strain shadows of IP+SP lithons and rare, poorly-formed σ- and δ- type objects (Fig. 4b). Rotation also occurs on the grain scale, evidenced by the higher proportion of equant SP retained to relatively high finite strain.

3.3. C' shear bands

C' shear bands were identified as shear bands that dip ≥15° in the direction of shear (opposite direction to S planes) with a synthetic, normal shear sense. They form in layers of WP (shear bands or shorter layers) as isolated bands within a microstructure dominated by S-C fabric (Figs. 5,6) or as C' arrays that form S-C' fabric within part of the model. Isolated C' shear bands are evident in almost all models, but S-C' fabrics only form in models with ≥15WP.

C' shear bands form when layers of WP parallel to the C plane rotate forwards. This occurs in two situations: (1) when strain rate increases in a discontinuous layer of WP (Fig. 5) or (2) when the tips of a shear band are separated by a "hard-phase bridge" that experiences high stress (Fig. 6). These observations and their meaning are discussed in section 4.3. C' shear bands are ephemeral, becoming inactive either due to (1) rotation backwards (anticlockwise in dextral shear) into parallelism with the C plane (Figs. 5d, 6d) or (2) shortening and "collapse" (Fig. 7). In the first process the C' shear band rapidly rotates backwards into parallelism with the C plane and undergoes a small degree of thickening and shortening (Figs. 5d, 6d). When this happens shortening may also occur in the IP+SP material under the plane resulting in small asymmetric folds. These folds nucleate with axial planes approximately parallel to the S plane, and gradually rotate and tighten as shearing progresses, eventually forming gently inclined to recumbent, isoclinal folds. Prolonged
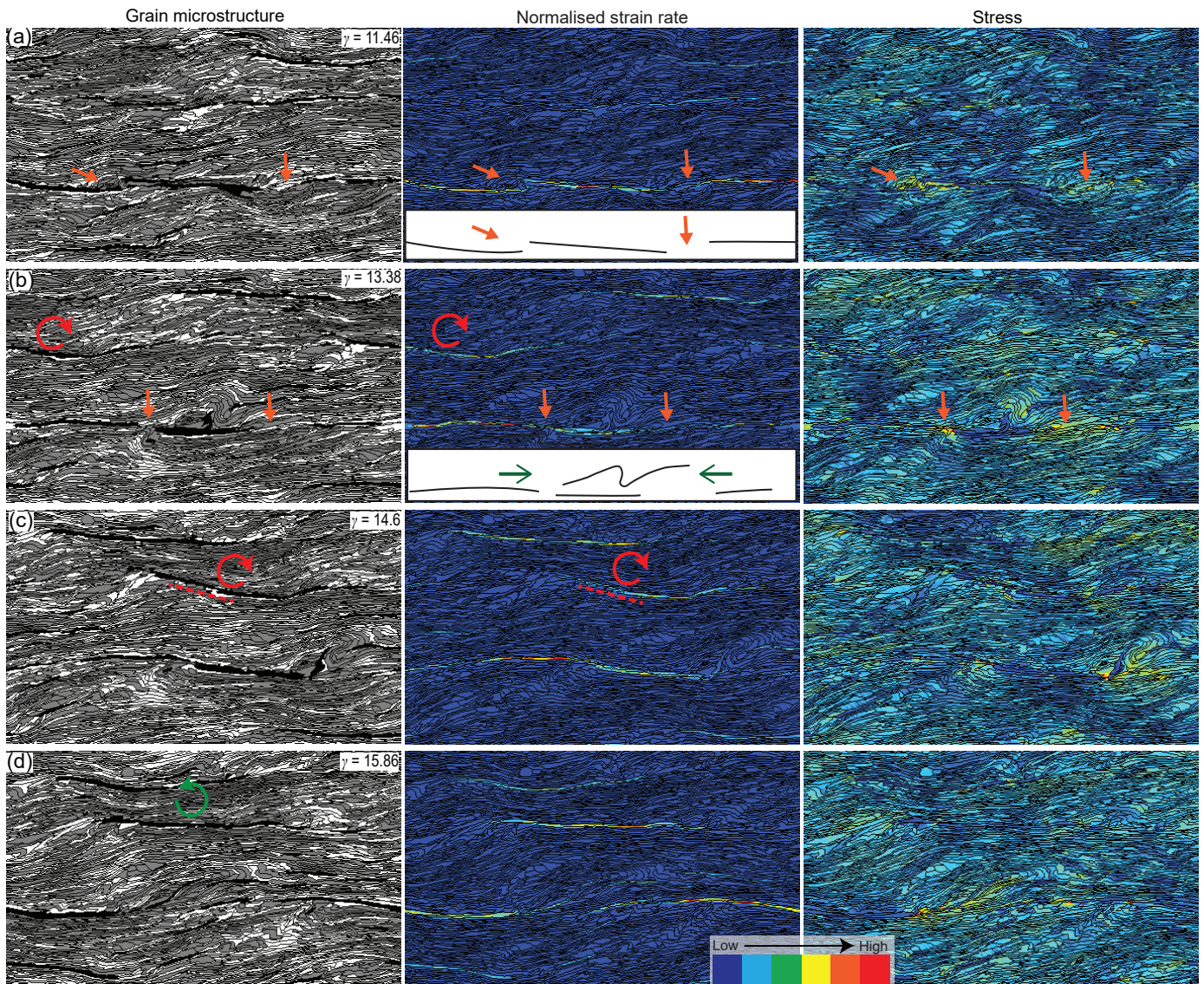
Fig. 6. The formation of C' shear bands by the rotation of a C plane forwards due to high stress in a "hard-phase bridge" within the shear band. (a) Two sections of a shear band are close to forming a continuous, through-going shear band but for sections that contain a high concentration of IP and SP, forming a hard-phase bridge (orange arrows). (b) High stress in the hard phase bridge (orange arrows) causes shortening and thickening of the shear band. The area above the shortened section of shear band also shortens forming asymmetric folds and a layer of WP begins to rotate forwards. Inset depicts major structures in model with orange arrows pointing to the high stress, low strain rate regions noted in the model above and green arrows denoting area of the shear band that has been shortened and thickened. (c) Rotated WP layer forms a C' shear band. (d) Once strain rate and stress have lowered in the shear band, the C' shear band rotates backwards into parallelism with the C plane. The first column shows the grain microstructure, the second column shows the normalised von Mises strain rate and the third column shows the von Mises stress. Model shown is 5WP_High and images in the same row correspond to the same model and step.

shearing on fold limbs generates rootless folds. The alternative fate of C' shear bands is that they shorten internally and collapse into triangle- and X- shaped patches of WP with their long axis at a high angle to the SZB (Fig. 7). The foliation around these patches is either pinched in towards the patch or isoclinally folded (Fig. 7). Occasionally these high-angle patches later become reactivated into C'' shear bands or they may be intersected by a shear band and sheared apart.

C' shear bands form in all models except 5WP_Low (Table 3). They are rare in the other 5WP models, with only 2-3 isolated C' shear bands forming over the simulation run. They are more common in the 15WP and 30WP models. In the 15WP models C' shear bands form at the same rate in the different strength contrast conditions until $\gamma = 12$. After this point the high strength contrast model shows a more heterogeneous distribution of strain rate than the other two models, and forms more C' shear bands. In the 30WP simulations the high strength contrast simulation shows a higher proportion of C' shear bands than the other 30WP simulations initially, but then develops a through-going shear band that partitions the majority of the strain, and C' shear bands no longer form. The 30WP simulations also develop an S-C' fabric in sections in the medium and high strength contrast simulations. In the 45WP simulations the strain rate distribution is
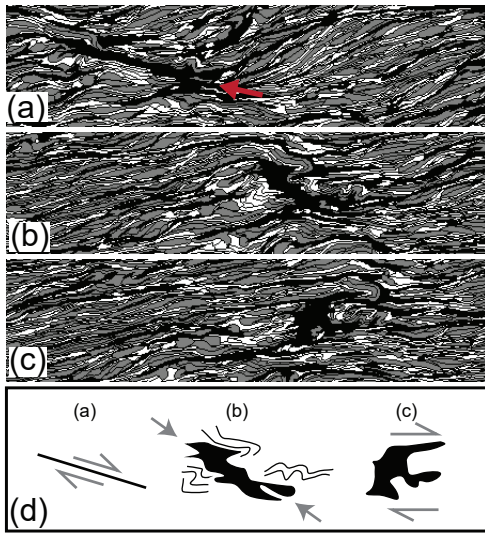
Fig. 7.The fate of C' shear bands. (a) C' shear band begins to shorten parallel to its length, and extend and thicken perpendicular to its length. (b) C' shear band is at a high angle to the foliation and has shortened. The layers of IP+SP on either side have folded. (c) The collapsed C' shear band is sheared and forms an asymmetrical X-type structure. (d) Interpretation of the main features shown in (a-c). The other fate of C' shear bands is that they rotate backwards into parallelism with the C plane, as depicted in Figs. 4d and 5d. Images taken from 30WP_Med model.

more heterogenous so while C' shear bands and S-C' fabric are still common they are active for shorter periods than in simulations with less WP.

To summarise, we find that C' shear bands form when there is 5% weak phase in conditions with a medium or high phase strength contrast. When there is 15 or 30% weak phase C' shear bands form at all phase strength contrast conditions. The simulations that contain 45% weak phase also form C' shear bands but they are short lived.

4. Discussion

In this section we interpret the numerical simulation results obtained, suggest possible processes that form C' shear bands and compare our data to previous studies. Numerical modelling allows insight into a developing microstructure at small strain increments, so it can provide valuable information about processes that have previously only been inferred in studies on experimentally- and naturally- deformed rocks. As such, after discussion of C' shear bands, we also examine the general microstructural development of the simulations.

4.1. Processes that form C' shear bands

In section 3.1.3 we described how the typical strain rate distribution is heterogeneous and dynamic. The locus of maximum strain rate moves between layers of WP to wherever shearing is easiest. C plane-parallel layers at a moderate strain rate may suddenly experience a high strain rate when shearing becomes difficult in another region of the model. This increase in strain rate raises stress at the tip of the WP layer, in the IP+SP. This results in displacement of the IP+SP, allowing grains of WP to link up and form shear bands (Holyoke and Tullis, 2006). If the stress is sufficiently high, the IP+SP can shorten and the layer of WP rotate forwards (Fig. S2), forming a C' shear band (Fig. 5). Once the C' shear band begins to rotate forwards its strain rate decreases since it is no longer at a favourable angle for shearing. In some simulations this results in a domino effect, where strain rate increases in a shear band causing it to rotate forwards, which forces strain to localise to a different shear band, resulting in forward rotation of that layer, and so on.

The other precursor to C' shear band rotation is zones of high stress in hard-phase bridges that separate tips of WP shear bands (Fig. 6). These hard-phase bridges typically show the highest stress within a model, which increases as the shear band lengthens and the bridge gets smaller (Fig. 6b). Eventually, the shear band either (i) connects up, forming a through-going shear band, (ii) folds, or (iii) a section of it rotates forwards, forming a C' shear band (Fig. 6). Rotating the shear band away from the C plane reduces the strain rate in the layer, reducing stress in the bridge. Heightened stress in hard-phase bridges can also cause shortening and folding in the IP+SP within the hard-phase bridge, which in turn causes the area above and below the gap to shorten (Fig. 6b). If there are layers of WP within this area they may shorten or else rotate forwards, forming a C' shear band (Fig. 6c).

Taken together, these results indicate that C' shear bands can form due to mechanical instabilities brought about by the heterogeneous distribution of strain rate and stress. These results are broadly consistent with previous research that has suggested that C' shear bands form when strain distribution is heterogeneous (Berthé et al., 1979, Goodwin and Tikoff, 2002, Holyoke and Tullis, 2006, Michibayashi and Murakami, 2007). However, our findings depart significantly from a number of previous suggestions about the inception and fate of C' shear bands. Before a comparison of these findings with previous research, a number of methodological differences between our study and those previous should be noted. First, we only look at the case

of deformation under simple shear (Wk = 1), whereas previous studies use rocks from shear zones that have experienced general shear (Wk < 1). A component of pure shear would certainly affect the development of C' shear bands, although our simulations show that it is not a necessary requirement to form C' shear bands (cf. de Riese et al., 2019). Additionally, our simulations show that the finite strain, proportion of weak phase, and strength contrast between phases are all important determinants of C' shear band inception and these factors are typically not determined in studies of natural shear zones. Finally, there are some important deformation processes that are not included in this series of simulations, including dynamic recrystallization, dehydration and hydrolytic weakening, and other dynamic feedback processes known to occur in shear zones (e.g., Johnson et al., 2008, Johnson et al., 2011, Oliot et al., 2014, Finch et al., 2016, Gardner et al., 2017). This means that we cannot expect results from natural and simulated shear zones to be identical; indeed the great benefit of simulations is the degree of control and the ability to model a wide range of ideal scenarios. Therefore, we compare our results to previous work with the caveat that some discrepancies between our findings may be a result of the differences listed above.

As described in section 1 previous experimental studies determined that C' shear bands are produced when the strength ratio between phases is at least 3-5 (Jordan, 1987, Stünitz and Tullis, 2001, Holtzman et al., 2003, Holyoke and Tullis, 2006) and the proportion of weak phase is >20% (in a two-phase aggregate; Jordan, 1987, Goodwin and Tikoff, 2002). Our findings provide additional constraints on the conditions in which these structures form. As described in section 3.3, we find that simulations with 15% and 30% weak phase produce the greatest number of C' shear bands. Simulations with 5% and 45% WP produce fewer C' shear bands and the 5WP_Low simulation produces none. Our results suggest that when the proportion of WP is <15%, stress and strain rate heterogeneities are insufficient to cause C planes to rotate forwards to form C' shear bands. Conversely, in the simulations with 45% WP strain partitions to the weak phase. The increase in heterogeneity increases the rate of rotation of WP layers forward and backwards, so C' shear bands are more transient, particularly when there is a high phase strength contrast. Llorens et al. (2016b; 2017) and de Riese et al. (2019) have shown that localisation of strain rate in C and C' orientations also occurs in pure, mechanically anisotropic aggregates (equivalent to 100WP here). However, in such materials (e.g., pure ice) shear bands may be hard to detect.

Previous studies have suggested that C' shear bands form on the plane of maximum shear strain rate (e.g., Platt and Vissers, 1980, Simpson and De Paor, 1993, Klepeis et al., 1999, Law et al., 2004, Kurz and Northrup, 2008, Gillam et al., 2013). Our results suggest that this is not the case because when C' shear bands form, the plane of maximum shear strain rate is parallel to the SZB. Our work also suggests that C' shear bands are not necessarily a result of general shear (Simpson and De Paor, 1993) or Coulomb failure (Blenkinsop and Treloar, 1995). Previous research has also suggested that C' shear bands form during the last stage of shear zone activity (Platt, 1984, Gillam et al., 2013). Our study shows that C' shear bands develop once there are WP layers that localise strain, which form at $\gamma \sim 2\text{-}3$ (at medium strength contrast). In contrast to previous studies, our results suggest that C' shear bands form due to stress and strain rate heterogeneities that are produced as a result of anisotropy within minerals (intrinsic anisotropy) and between minerals (composite anisotropy). We do not employ strain weakening mechanisms, but rather show that these structures can develop as a natural result of mechanical anisotropy, consistent with the results of Griera et al. (2013), Ran et al., (2019) and Gomez-Rivas and Greira (2012) who demonstrate that anisotropy is an important determinant of structural evolution.

Our modelling also provides unique insight into the fate of C' shear bands. As described in section 3.3, we find that C' shear bands either rotate backwards into parallelism with the SZB or shorten and collapse. When the latter occurs, they form triangle- and X- shaped structures that appear similar to the structures that form during foliation boudinage in Platt and Vissers (1980) and Gillam et al. (2013). Platt and Vissers (1980) describe the formation of those structures as a result of extension parallel to the foliation, which opens fractures that have a long axis perpendicular to the foliation. Our results show that the same types of structures can form when ductile shear bands are rotated to high angles with the foliation. When C' shear bands approach angles higher than ~35° they presumably enter the shortening field. This causes shortening parallel to their length and extension perpendicular, producing triangle- and X- shaped structures (Fig.

7). This may explain why C' shear bands are not found at angles > 35° to the SZB.

However, not all C' shear bands undergo shortening parallel to their length, as some rotate backwards into parallelism with the C plane. The fate of C' shear bands may be controlled by the timing of changes in stress or strain rate relative to the degree of rotation of the C' shear band. C' shear bands appear to rotate forwards until there is a change in the stress or strain rate (e.g., see supplementary material strain rate and grain microstructure movies for 15WP_Med condition at ~00:50). We suggest that if this change occurs before the C' shear band rotates into the shortening field, the C' shear band will simply rotate back into parallelism with the SZB. However, if this change does not occur the C' shear band will continue rotating forwards, enter the shortening field, and collapse and thicken, forming X- and triangle- shaped structures filled with WP.

4.2. Microstructural evolution: a comparison to previous research
The microstructural development of these simulations is controlled by the WP and the extent to which it is interconnected and parallel to the SZB. This factor controls the distribution of strain rate and the locus of maximum stress (e.g., Figs. 5a,b and 6a,b). In turn, the distribution of stress and strain rate determines the microstructures that develop, including the development of S-C fabric, C-parallel shear bands, C' shear bands, and C" shear bands. This dependence of the developing microstructure on the interconnectedness of the WP was first highlighted by Handy (1990, 1994) who suggested that the transition from a load-bearing framework to an interconnected weak phase represented a shift in the way a polyphase rock deforms. We find that this transition is important, however, we also find that the weak phase has a significant effect on microstructural development even before it is interconnected (see also Bons and Cox, 1994; Jessell et al., 2009; Dabrowski et al., 2012; Llorens et al., 2019). Early stages of shearing are dominated by antithetic shear bands on short layers of WP in simulations with ≥15% WP and the majority of WP grains are parallel to the SZB by $\gamma = 2$ in simulations with ≤30% WP. Once parallel to the SZB they partition strain rate. Handy (1994) found that stress concentrates in the load-bearing framework but once an interconnected WP forms, stress is sometimes higher in the WP than the SP. We do not find this to be the case in any of our simulations. Stress is always concentrated in the SP+IP, and is highest in the regions adjacent to WP that are at a high strain rate. Handy (1994) also suggested that the degree of stress and strain partitioning depends on the strength contrast and relative amounts of WP and SP. We find that strain localises to the WP irrespective of its proportion, however, it may be that we did not use a proportion of WP low enough to allow development of a load bearing framework.

Since the foundational work of Jordan (1987) and Handy (1990, 1994) many others have found that the interconnectedness of the weak phase is the most significant factor governing deformation style in naturally- and experimentally- deformed shear zone rocks (e.g., Handy et al., 1999, Goodwin and Tikoff, 2002, Holyoke and Tullis, 2006, Gonçalves et al., 2015, Jammes et al., 2015; Hunter et al., 2016, Gardner et al., 2017; Llorens et al., 2019). Consistent with the findings of Holyoke and Tullis (2006), we find that the mechanism that allows the weak phase to link up is high stress in SP and IP at the tips of WP grains, which causes SP and IP to flow. This effect is particularly pronounced when WP forms C planes that localise strain rate. Beyond this feature, the evolution of our simulations agrees with the literature more broadly, where similar stages of microstructural development have been proposed including an initial stage of grain elongation parallel to the S plane, rotation of fabric elements to the C plane, and strain localisation to the weakest phase parallel to the C plane (e.g., Berthé et al., 1979, Jordan, 1987). More broadly we note that shear bands in our models lengthen by the same process as that observed in natural shear zones at every scale, that is by the linking of segments due to the accumulation of strain and displacement (e.g., Fossen and Cavalcante, 2017).

This work also provides insight into the genesis of antithetic C" shear bands. We show that these structures develop at the start of the simulation before C planes have been established (at $\gamma < 2$) as well as in simulations with a high proportion of weak phase and a high strength contrast at high values of finite strain. They form as a result of rotation of clusters of SP±IP that behave as competent lithons. These lithons rotate clockwise between C planes with antithetic shear bands accommodating the vertical component of rotation. As such, antithetic shear zones accommodate deformation in regions of high vorticity within the model.

These results are consistent with those of Ran et al. (2018) who found that vertical antithetic C" shear bands formed in the weak matrix at the margins of a strong phase and that the number of C" shear bands was positively correlated with the strong phase proportion and viscosity ratio.

All simulations in this study use a simple shear boundary condition and yet the structures that develop are highly variable within and between simulations, with the formation of distinct and dynamic deformation domains that variably show passive rotation, stretching, or shortening. This is consistent with the work of Jiang (1994) and Jiang and White (1995) who found that in polyphase materials the microstructures that develop within a shear zone are complex and do not show a simple relationship with the boundary conditions. In our simulations complexity in deformation style in the SP and IP was a result of the strength contrast between phases as well as the context of the phases. Grains of IP and SP could be flattened parallel to the SZB in one section of the simulation, but equant and relatively undeformed in another (Figs. 2b,c). Furthermore, grains of IP and SP could form lithons that deform as one domain (similar to transient pebble clusters in Ran et al., 2018), forming microstructures that approximate σ- and δ- objects (Fig. 4b). This study highlights the importance of structural domains in rocks with strong strain localisation and suggests that a given mineral may show different apparent competence on the scale of microns, depending on its context. It also suggests that approaches that use isolated microstructural features to infer aspects of bulk deformation or strain are problematic. For example, the angle between the principal extension direction and the SZB (θ) has a systematic relationship with finite strain, highlighted by Ramsay and Graham (1970) as follows:

$$\tan 2\theta = 2/\gamma \qquad\qquad\qquad (3)$$

This relationship is often used to determine strain and total displacement on the shear zone through measurement of θ between C planes and rotated markers, such as dykes (e.g., Finch et al., 2014) or the S plane. Our study suggests that the angle between the SZB and mineral phases or structural features depends on the strength of the phase, the contrast between the phase in question and other phases within the rock, and the distribution of strain rate and stress within the model. Our work demonstrates that a layer of WP that has rotated into parallelism with the SZB may later rotate synthetically or antithetically out of parallelism. Caution is advised when using this method to estimate finite strain, even in shear zones with a simple shear boundary condition.

5. Conclusions

We investigated the mechanisms for the development of C' shear bands in three-phase numerical models with varying phase strength contrasts and proportions of weak phase. We found that C' shear bands form when there is 5% weak phase in conditions with a medium or high phase strength contrast. When there is 15 or 30% weak phase C' shear bands form at all phase strength contrasts. The simulations that contain 45% weak phase also form C' shear bands but they are short lived. C' shear bands form when layers of WP parallel to the C plane rotate forwards (clockwise) by 15-35° and they are destroyed when they rotate backwards or when they shorten and form X- or triangle- shaped structures at a high angle to the SZB. Rotation of C planes forwards is controlled by the local stress and strain rate fields which produce mechanical instabilities in the microstructure. C' shear bands form in low strain rate and stress layers of WP, not on the plane of maximum strain rate as has been previously suggested. Our simulations also provide insight into the processes during strain localisation and partitioning in shear zones. Strain rate partitions to layers of interconnected weak phase and there are regions within the simulations that variably undergo shortening, extension, and rotation despite use of the same boundary conditions for all simulations. This highlights the importance of phase strength contrast and local strain and stress fluctuations in controlling the developing microstructure. Using a non-linear, anisotropic, viscous model with heterogenous distributions of grains, we are able to reproduce the main structures found in mylonites including S-C fabrics, C' and C" shear bands, as well as a variable spatial and temporal evolution of strain localisation. We do not use strain weakening functions in the models, instead strain localisation develops as a natural consequence of heterogeneities related to phase distribution and the anisotropy of the weak phase (composite and intrinsic anisotropy, respectively).

Acknowledgements

References

Berthé, D., Choukroune, P. and Jegouzo, P., 1979. Orthogneiss, mylonite and non coaxial deformation of granites: the example of the South Armorican Shear Zone. Journal of Structural Geology 1(1), 31-42.

Blenkinsop, T. G. and Treloar, P. J., 1995. Geometry, classification and kinematics of S-C and S-C′ fabrics in the Mushandike area, Zimbabwe. Journal of Structural Geology 17(3), 397-408.

Bobyarchick, A. R., 1986. The eigenvalues of steady flow in Mohr space. Tectonophysics 122(1–2), 35-51.

Bons, P. D. and Cox, S. J. D., 1994. Analogue experiments and numerical modelling on the relation between microgeometry and flow properties of polyphase materials. Materials Science and Engineering A175, 237-245.

Bons, P. D., Koehn, D. and Jessell, M. W., 2008. Microdynamics Simulation. In: Lecture Notes in Earth Sciences (edited by Bhattacharji, S., Neugebauer, H. J., Reitner, J. & Stüwe, K.) 106. Springer-Verlag, Berlin, 405.

Cyprych, D., Brune, S., Piazolo, S. and Quinteros, J., 2016. Strain localization in polycrystalline material with second phase particles: Numerical modeling with application to ice mixtures. Geochemistry, Geophysics, Geosystems 17, 1-21.

de Riese, T., Evans, L., Gomez-Rivas, E., Griera, A., Lebensohn, R.A., Llorens, M.-G., Ran, H., Sachau, T., Weikusat, I., Bons, P.D., 2019. Shear localisation in anisotropic, non-linear viscous materials that develop a CPO: A numerical study. Journal of Structural Geology 124, 81-90.

Dabrowski, M., Schmid, D.W., Podladchikov, Y.Y., 2012. A two-phase composite in simple shear: Effective mechanical anisotropy development and localization potential. Journal of Geophysical Research 117, B08406.

Delle Piane, C., Wilson, C. J. L. and Burlini, L., 2009. Dilatant plasticity in high-strain experiments on calcite–muscovite aggregates. Journal of Structural Geology 31(10), 1084-1099.

Dennis, A. J. and Secor, D. T., 1987. A model for the development of crenulations in shear zones with applications from the Southern Appalachian Piedmont. Journal of Structural Geology 9(7), 809-817.

Dillamore, I. L., Roberts, J. G. and Bush, A. C., 1979. Occurrence of shear bands in heavily rolled cubic metals. Metal Science 13(2), 73-77.

Finch, M., Hasalová, P., Weinberg, R. F. and Fanning, C. M., 2014. Switch from thrusting to normal shearing in the Zanskar shear zone, NW Himalaya: Implications for channel flow. Geological Society of America Bulletin 126(7-8), 892-924.

Finch, M. A., Weinberg, R. F., Hasalová, P., Becchio, R., Fuentes, M. G. and Kennedy, A., 2017. Tectono-metamorphic evolution of a convergent back-arc: the Famatinian orogen, Sierra de Quilmes, Sierras Pampeanas, NW Argentina. Geological Society of America Bulletin 129(11-12), 1602-1621.

Finch, M. A., Weinberg, R. F. and Hunter, N. J. R., 2016. Water loss and the origin of thick ultramylonites. Geology 44(8), 599-602.

Fossen, H. and Cavalcante, G. C. G., 2017. Shear zones – A review. Earth-Science Reviews 171, 434-455.

Gardner, R. L., Piazolo, S., Daczko, N. R. and Evans, L., 2019. Ductile deformation without localization: insights from numerical modeling. Geochemistry, Geophysics, Geosystems, 20.

Gardner, R., Piazolo, S., Evans, L. and Daczko, N., 2017. Patterns of strain localization in heterogeneous, polycrystalline rocks – a numerical perspective. Earth and Planetary Science Letters 463, 253-265.

Gillam, B. G., Little, T. A., Smith, E. and Toy, V. G., 2013. Extensional shear band development on the outer margin of the Alpine mylonite zone, Southern Alps, New Zealand. Journal of Structural Geology 54, 1-20.

Gomez-Rivas, E., Bons, P. D., Griera, A., Carreras, J., Druguet, E. and Evans, L., 2007. Strain and vorticity

analysis using small-scale faults and associated drag folds. Journal of Structural Geology 29(12), 1882-1899.

Gomez-Rivas E. and Griera, A., Shear fractures in anisotropic ductile materials: an experimental approach, J. Struct. Geol. 34, 2012, 61-76.

Gomez-Rivas, E., Griera, A., Llorens, M.-G., Bons, P.D., Lebensohn, R. and Piazolo, S. 2017. Subgrain rotation recrystallization during shearing: insights from full-field numerical simulations of halite polycrystals. Journal of Geophysical Research Solid Earth, 122 (11), 8810–8827.

Gonçalves, C. C., Gonçalves, L. and Hirth, G., 2015. The effects of quartz recrystallization and reaction on weak phase interconnection, strain localization and evolution of microstructure. Journal of Structural Geology 71, 24-40.

Goodwin, L. B. and Tikoff, B., 2002. Competency contrast, kinematics, and the development of foliations and lineations in the crust. Journal of Structural Geology 24(6–7), 1065-1085.

Grasemann, B., Stüwe, K. and Vannay, J.-C., 2003. Sense and non-sense of shear in flanking structures. Journal of Structural Geology 25(1), 19-34.

Griera, A., Bons, P. D., Jessell, M. W., Lebensohn, R. A., Evans, L. and Gomez-Rivas, E., 2011. Strain localization and porphyroclast rotation. Geology 39, 275-278.

Griera, A., Llorens, M.-G., Gomez-Rivas, E., Bons, P. D., Jessell, M. W., Evans, L. and Lebensohn, R. A., 2013. Numerical modelling of porphyroclast and porphyroblast rotation in anisotropic rocks. Tectonophysics 587, 4-29.

Handy, M. R., 1990. The solid-state flow of polymineralic rocks. Journal of Geophysical Research: Solid Earth 95(B6), 8647-8661.

Handy, M. R., 1994. Flow laws for rocks containing two non-linear viscous phases: A phenomenological approach. Journal of Structural Geology 16(3), 287-301.

Handy, M. R., Wissing, S. B. and Streit, L. E., 1999. Frictional–viscous flow in mylonite with varied bimineralic composition and its effect on lithospheric strength. Tectonophysics 303(1–4), 175-191.

Holtzman, B. K., Groebner, N. J., Zimmerman, M. E., Ginsberg, S. B. and Kohlstedt, D. L., 2003. Stress-driven melt segregation in partially molten rocks. Geochemistry, Geophysics, Geosystems 4(5).

Holtzman, B. K. and Kohlstedt, D. L., 2007. Stress-driven Melt Segregation and Strain Partitioning in Partially Molten Rocks: Effects of Stress and Strain. Journal of Petrology 48(12), 2379-2406.

Holyoke, C. W. and Tullis, J., 2006. Mechanisms of weak phase interconnection and the effects of phase strength contrast on fabric development. Journal of Structural Geology 28(4), 621-640.

Hunter, N. J. R., Hasalová, P., Weinberg, R. F. and Wilson, C. J. L., 2016. Fabric controls on strain accommodation in naturally deformed mylonites: The influence of interconnected micaceous layers. Journal of Structural Geology 83, 180-193.

Jammes, S., Lavier, L. L. and Reber, J. E., 2015. Localization and delocalization of deformation in a bimineralic material. Journal of Geophysical Research: Solid Earth 120(5), 3649-3663.

Jessell, M. W., Bons, P. D., Evans, L., Barr, T. and Stüwe, K., 2001. Elle: a micro-process approach to the simulation of microstructures. Computers and Geosciences 27, 17-30.

Jessell, M. W., Bons, P. D., Griera, A., Evans, L. and Wilson, C. J. L., 2009. A tale of two viscosities. Journal of Structural Geology 31, 719-736.

Ji, S., Jiang, Z., Rybacki, E., Wirth, R., Prior, D. and Xia, B., 2004. Strain softening and microstructural evolution of anorthite aggregates and quartz–anorthite layered composites deformed in torsion. Earth and Planetary Science Letters 222(2), 377-390.

Jiang, D., 1994. Vorticity determination, distribution, partitioning and the heterogeneity and non-steadiness of natural deformations. Journal of Structural Geology 16(1), 121-130.

Jiang, D. and White, J. C., 1995. Kinematics of rock flow and the interpretation of geological structures, with particular reference to shear zones. Journal of Structural Geology 17(9), 1249-1265.

Johnson, S. E., Jin, Z.-H., Naus-Thijssen, F. M. J. and Koons, P. O., 2011. Coupled deformation and metamorphism in the roof of a tabular midcrustal igneous complex. Geological Society of America Bulletin 123(5-6), 1016-1032.

Johnson, S. E., Marsh, J. H. and Vernon, R. H., 2008. From tonalite to mylonite: Coupled mechanical and chemical processes in foliation development and strain localization. Journal of the Virtual Explorer 30.

Jordan, P. G., 1987. The deformational behaviour of bimineralic limestone-halite aggregates. Tectonophysics 135(1–3), 185-197.

Klepeis, K. A., Daczko, N. R. and Clarke, G. L., 1999. Kinematic vorticity and tectonic significance of superposed mylonites in a major lower crustal shear zone, northern Fiordland, New Zealand. Journal of Structural Geology 21(10), 1385-1405.

Kurz, G. A. and Northrup, C. J., 2008. Structural analysis of mylonitic rocks in the Cougar Creek Complex, Oregon–Idaho using the porphyroclast hyperbolic distribution method, and potential use of SC′-type extensional shear bands as quantitative vorticity indicators. Journal of Structural Geology 30(8), 1005-1012.

Law, R. D., Searle, M. P. and Simpson, R. L., 2004. Strain, deformation temperatures and vorticity of flow at the top of the Greater Himalayan Slab, Everest Massif, Tibet. Journal of the Geological Society 161(2), 305-320.

Lebensohn, R. A., 2001. N-site modeling of a 3D viscoplastic polycrystal using fast Fourier transform. Acta Materialia 49, 2723-2737.

Lebensohn, R. A., Brenner, R., Castelnau, O. and Rollett, A. D., 2008. Orientation image-based micromechanical modelling of subgrain texture evolution in polycrystalline copper. Acta Materialia 56, 3914-3926.

Lebensohn, R. A., Montagnat, M., Mansuy, P., Duval, P., Meysonnier, J. and Philip, A., 2009. Modeling viscoplastic behavior and heterogeneous intracrystalline deformation of columnar ice polycrystals. Acta Materialia 57(5), 1405-1415.

Little, T. A., Hacker, B. R., Gordon, S. M., Baldwin, S. L., Fitzgerald, P. G., Ellis, S. and Korchinski, M., 2011. Diapiric exhumation of Earth's youngest (UHP) eclogites in the gneiss domes of the D'Entrecasteaux Islands, Papua New Guinea. Tectonophysics 510(1–2), 39-68.

Llorens, M.-G., Griera, A., Bons, P. D., Lebensohn, R. A., Evans, L. A., Jansen, D. and Weikusat, I., 2016a. Full-field predictions of ice dynamic recrystallisation under simple shear conditions. Earth and Planetary Science Letters 450, 233-242.

Llorens, M.-G., Griera, A., Bons, P. D., Roessiger, J., Lebensohn, R. A., Evans, L. and Weikusat, I., 2016b. Dynamic recrystallisation of ice aggregates during co-axial viscoplastic deformation: a numerical approach. Journal of Glaciology 62(232), 359-377.

Llorens, M.-G., Griera, A., Steinbach, F., Bons, P.D., Gomez-Rivas, E., Jansen, D., Lebensohn, R. and Weikusat, I., 2017. Dynamic recrystallisation during deformation of polycrystalline ice: insights from numerical simulations. Philosophical Transactions of the Royal Society A, 375:20150346.

Llorens, M.-G., Gomez-Rivas, E., Ganzhorn, A.-C., Griera, A., Steinbach, F., Roessiger, J., Labrousse, L., Walte, N., Weikusat, I. and Bons, P.D. 2019. The effect of dynamic recrystallisation on the rheology and microstructures of partially molten rocks. Journal of Structural Geology, 118, 224-235.

Meyer, S. E., Kaus, B. J. P. and Passchier, C., 2017. Development of branching brittle and ductile shear zones: A numerical study. Geochemistry, Geophysics, Geosystems 18(6), 2054-2075.

Michibayashi, K. and Murakami, M., 2007. Development of a shear band cleavage as a result of strain partitioning. Journal of Structural Geology 29(6), 1070-1082.

Montagnat, M., Castelnau, O., Bons, P. D., Faria, S. H., Gagliardini, O., Gillet-Chaulet, F., Grennerat, F., Griera, A., Lebensohn, R. A., Moulinec, H., Roessiger, J. and Suquet, P., 2014. Multiscale modeling of ice deformation behavior. Journal of Structural Geology 61, 78-108.

Oliot, E., Goncalves, P., Schulmann, K., Marquer, D. and Lexa, O., 2014. Mid-crustal shear zone formation in granitic rocks: Constraints from quantitative textural and crystallographic preferred orientations analyses. Tectonophysics 612–613, 63-80.

Passchier, C. W., 1991. Geometric constraints on the development of shear bands in rocks. Geologie en Mijnkouw 70(2), 203-211.

Pennacchioni, G. and Mancktelow, N. S., 2007. Nucleation and initial growth of a shear zone network within compositionally and structurally heterogeneous granitoids under amphibolite facies conditions. Journal of Structural Geology 29(11), 1757-1780.

Platt, J. P., 1984. Secondary cleavages in ductile shear zones. Journal of Structural Geology 6(4), 439-442.

Platt, J. P. and Vissers, R. L. M., 1980. Extensional structures in anisotropic rocks. Journal of Structural Geology 2(4), 397-410.

Ramsay, J. G. and Graham, R. H., 1970. Strain variation in shear belts. Canadian Journal of Earth Science 7, 786 - 813.

Ramsay, J. G. and Lisle, R. J., 2000. The Techniques of Modern Structural Geology. Academic Press, London.

Ran, H., Bons, P. D., Wang, G., Steinbach, F., Finch, M. A., Griera, A., Gomez-Rivas, E., Llorens, M.-G., Ran, S. and Liang, X., 2018. High-strain deformation of conglomerates: Numerical modelling, strain analysis, and an example from the Wutai Mountains, North China Craton. Journal of Structural Geology 114, 222-234.

Ran, H., de Riese, T., Llorens, M.-G., Finch, M. A., Evans, L. A., Gomez-Rivas, E., Griera, A., Jessell, M. W., Lebensohn, R. A., Piazolo, S. and Bons, P. D., 2019. Time for anisotropy: The significance of mechanical anisotropy for the development of deformation structures. Journal of Structural Geology 125, 41-47.

Rosenberg, C. L. and Handy, M. R., 2005. Experimental deformation of partially melted granite revisited: implications for the continental crust. Journal of Metamorphic Geology 23(1), 19-28.

Simpson, C. and De Paor, D. G., 1993. Strain and kinematic analysis in general shear zones. Journal of Structural Geology 15(1), 1-20.

Steinbach, F., Bons, P. D., Griera, A., Jansen, D., Llorens, M.-G., Roessiger, J. and Weikusat, I., 2016. Strain localisation and dynamic recrystallisation in the ice-air aggregate: a numerical study. The Cryosphere 10, 3071-3089.

Stünitz, H. and Tullis, J., 2001. Weakening and strain localization produced by syn-deformational reaction of plagioclase. International Journal of Earth Sciences : Geologische Rundschau 90(1), 136-148.

White, S., 1979. Large strain deformation: report on a tectonic studies group discussion meeting held at Imperial College, London on 14 November 1979. Journal of Structural Geology 1(4), 333-339.

Williams, P. F. and Price, G. P., 1990. Origin of kinkbands and shear-band cleavage in shear zones: an experimental study. Journal of Structural Geology 12(2), 145-164.

Wilson, C. J. L., 1984. Shear bands, crenulations and differentiated layering in ice-mica models. Journal of Structural Geology 6(3), 303-319.

Xypolias, P., 2010. Vorticity analysis in shear zones: A review of methods and applications. Journal of Structural Geology 32(12), 2072-2092.